International Journal of Plasticity 89 (2017) 130–149

Contents lists available at ScienceDirect

International Journal of Plasticity

journal homepage: www.elsevier.com/locate/ijplas

A unified constitutive model for asymmetric tension and compression creep-ageing behaviour of naturally aged Al-Cu-Li alloy

Yong Li [a], Zhusheng Shi [a], Jianguo Lin [a, *], Yo-Lun Yang [a], Qi Rong [a], Bo-Ming Huang [b], Tsai-Fu Chung [b], Cheng-Si Tsao [b], Jer-Ren Yang [b], Daniel S. Balint [a]

[a] Department of Mechanical Engineering, Imperial College London, London SW7 2AZ, UK
[b] Department of Material Science and Engineering, National Taiwan University, Taiwan

ARTICLE INFO

Article history:
Received 24 August 2016
Received in revised form 31 October 2016
Accepted 18 November 2016
Available online 19 November 2016

Keywords:
Creep age forming
Ageing
Microstructures
Constitutive behaviour
Numerical algorithms

ABSTRACT

A set of unified constitutive equations is presented that predict the asymmetric tension and compression creep behaviour and recently observed double primary creep of pre-stretched/naturally aged aluminium-cooper-lithium alloy AA2050-T34. The evolution of the primary micro- and macro-variables related to the precipitation hardening and creep deformation of the alloy during creep age forming (CAF) are analysed and modelled. Equations for the yield strength evolution of the alloy, including an initial reversion and subsequent strengthening, are proposed based on a theory of concurrent dissolution, re-nucleation and growth of precipitates during artificial ageing. We present new observations of so-called double primary creep during the CAF process. This phenomenon is then predicted by introducing effects of interacting microstructures, including evolving precipitates, diffusing solutes and dislocations, into the sinh-law creep model. In addition, concepts of threshold creep stress σ_{th} and a microstructure-dependant creep variable H, which behave differently under different external stress directions, are proposed and incorporated into the creep model. This enables prediction of the asymmetric tension and compression creep-ageing behaviour of the alloy. Quantitative transmission electron microscopy (TEM) and related small-angle X-ray scattering (SAXS) analysis have been carried out for selected creep-aged samples to assist the development and calibration of the constitutive model. A good agreement has been achieved between the experimental results and the model. The model has the potential to be applied to creep age forming of other heat-treatable aluminium alloys.

* Corresponding author.
E-mail address: jianguo.lin@imperial.ac.uk (J. Lin).

http://dx.doi.org/10.1016/j.ijplas.2016.11.007

Nomenclature

Variables	Unit	Specification
c,c_0, Q, c_a, c_s	wt%	Solute concentration in the matrix, its initial value, equilibrium value and equilibrium values at ageing temperature and solution heat treatment temperature respectively
$\overline{c}$, $\overline{c}_0$, $\overline{c}_a$	–	Normalised solute concentration, its initial value and equilibrium value at ageing temperature
f, f_c, f_r	–	Volume fraction of precipitates, saturated value and relative value respectively
H	–	Microstructure dependant creep variable
r, r_d, r_n	nm	Precipitate radius, and radius of dissolving and new precipitates respectively
$\overline{r}$, $\overline{r}_d$, $\overline{r}_n$	–	Normalised r, r_d and r_n respectively
$\overline{r}_{d_0}$, $\overline{r}_{n_0}$	–	Initial values of $\overline{r}_d$ and $\overline{r}_n$
r_c	nm	Critical radius of precipitates at the peak-ageing state
r_e	nm	Equivalent radius of the matrix cell in the alloy
t	h	Time
T	K	Temperature
β	–	Yield strength contribution coefficient from dissolving precipitates and new precipitates
ε_{cr}, ε^p	–	Creep strain and plastic strain respectively
ρ, ρ_i, ρ_s	m^{-2}	Dislocation density and its initial and saturated values respectively
$\overline{\rho}$	–	Normalised dislocation density
σ, σ_{ea}	MPa	Applied and effective applied stress respectively
σ_A, σ_B	MPa	Contribution to precipitation hardening from shearing precipitates and bypass precipitates respectively
σ_{dis}, σ_p, σ_{ss}	MPa	Contribution from dislocations, precipitates and solid solution to yield strength respectively
σ_{p-d}, σ_{p-n}	MPa	Contribution to yield strength from dissolving precipitates and new precipitates respectively
σ_{th_0}	MPa	Initial threshold creep stress of AA2050-T34
σ_y	MPa	Yield strength

1. Introduction

Creep age forming (CAF) is a sheet metal forming technique originally developed for manufacturing large light weight and high performance stiffened panels in the aerospace industry (Holman, 1989). The process concurrently shapes and heat-treats aluminium alloys under external loading at elevated temperature by corresponding creep and artificial ageing mechanisms (Zhan et al., 2011a). Both deformation and age hardening phenomena occur and interact with each other during the process, which play a decisive role in determining springback and the mechanical properties of the formed alloys after CAF (Ho et al., 2004). Aluminium-Copper-Lithium alloy 2050 (AA2050), which can achieve excellent strength-ductility performance by artificial ageing, has great potential for aerospace applications (Lequeu et al., 2010). With an initial temper of T34 (solution heat treated, stretched to 3.5–4.5% and then naturally aged), the alloy can be stably stored at room temperature and has the capability to be significantly strengthened by further artificial ageing, making it a good candidate for the CAF process. Recently, new creep-ageing features of the alloy have been observed at 155 °C, including a double primary creep phenomenon with five creep stages, asymmetric creep-ageing behaviour under different loading directions and yield strength variations with an initial reversion (Li et al., 2016a). The aim of this study is to develop a model that captures the relevant mechanisms of creep-ageing of AA2050-T34 alloy in order to accurately predict its behaviour during CAF, and assist with potential industrial applications.

Over recent decades, modelling of creep deformation and age hardening of aluminium alloys has drawn considerable interest. Basic power-law equations have been widely used to predict the minimum creep strain rate of alloys under steady-state creep (Kim et al., 2016; Seidman et al., 2002; Zhao et al., 2015), while extended power-law, sinh-law and Orowan equations (Basirat et al., 2012; Huang et al., 2011; Kowalewski et al., 1994; Li et al., 2010; Lin, 2003; Zolochevsky and Voyiadjis, 2005) have all been applied to describe the evolution of creep strain, mainly its primary and tertiary stages, by introducing physical and/or phenomenal work hardening and damage variables into the equations. The θ projection method has also been used to model creep behaviour of particle-hardened alloys (Evans, 2000), predicting the hardening, recovery and damage phenomena of creep by taking corresponding internal variables as scalar quantities. Meanwhile, dislocation cutting and bypassing have been generally used to explain and model age hardening phenomena (Collins and Stone, 2014; Esmaeili et al., 2003b; Lin and Liu, 2003; Shercliff and Ashby, 1990). Shercliff and Ashby (1990) have modelled the evolution of yield strength during artificial ageing of aluminium alloys in a systematic way by relating internal state variables, such as precipitate radius and solute concentration, to the corresponding age hardening phenomenon. With increasing knowledge of the evolution of microstructural variables and their corresponding contributions to the yield strength of aluminium alloys during ageing, these process models have been further extended to predict resultant yield strength of aluminium alloys with different compositions (Esmaeili et al., 2003b; Liu et al., 2003) and initial heat treatment conditions, such as as-quenched (Raeisinia et al., 2006), naturally-aged (Esmaeili et al., 2003a) and over-aged (Starink and Wang, 2003) conditions.

For the CAF process, however, a unified constitutive model which can predict concurrent creep deformation and age hardening phenomena (creep-ageing behaviour) in both the primary and steady-state creep stages is needed. Some prior efforts have been made to develop unified constitutive models specifically for the CAF process. Ho et al. (2004) developed a unified model to relate microstructural variables to both creep and ageing phenomena, successfully predicting creep deformation, age hardening and springback of 7000-series aluminium alloys during the CAF process. Similar models have also been proposed by Li et al. (2010) and Zhang et al. (2013). Furthermore, Zhan et al. (2011b) have advanced the model for CAF of AA7055

by introducing normalised microstructural variables, thus simplifying the model, and good results have been achieved. Lam et al. (2015) applied this model to the finite element analysis of creep-ageing of AA2219 and successfully predicted spring-back of the alloy during the CAF process. However, existing models mainly considered dislocation hardening and recovery in the creep rate equation, which cannot fully explain and predict the recently observed double primary creep feature and the asymmetric tensile and compressive creep behaviour of AA2050-T34. The latter phenomenon has also been reported in other aluminium alloys (El-Shennawy et al., 1999; Zhang et al., 2015; Zolochevsky and Voyiadjis, 2005) and was attributed to the easier cavity nucleation under tensile creep-ageing condition or anisotropic strain hardening under tension and compression.

This study presents the first unified constitutive model that can predict both the evolution of yield strength hardening with an initial reversion, the double primary creep feature and asymmetric tension and compression creep behaviour of AA2050-T34 during creep-ageing. The evolution of three main internal microstructural variables – dislocation density, precipitate radius and solute concentration – and their contributions to age hardening and asymmetric creep behaviour are analysed and modelled based on fundamental creep and ageing theories. Quantitative transmission electron microscopy (TEM) and related small-angle X-ray scattering (SAXS) analysis of selected creep-aged samples of AA2050-T34 have been carried out to help develop and calibrate the corresponding microstructural equations. Finally, the model predictions of yield strength and creep strain evolution have been discussed and compared with the experiments.

2. Asymmetric creep-ageing behaviour of Al-Cu-Li alloy with double primary creep feature

A particular asymmetric creep-ageing behaviour with a new double primary creep feature was observed in an Al-Cu-Li alloy (AA2050-T34) in an earlier study (Li et al., 2016a). Fig. 1 illustrates the creep strain results under 150 MPa for both tension and compression: the creep strain in tension was found to be 1.5 to 3 times larger than in compression. The double primary creep feature, rather than conventional primary and steady state creep behaviour, was first observed in aluminium alloys during creep-ageing, where two primary creep stages with decreasing creep strain rates occur, as shown in Fig. 1. More details of the experimental setup and results can be found in (Li et al., 2016a).

Fig. 2 shows schematically the evolution of precipitates during creep-ageing of the alloy (Decreus et al., 2013; Li et al., 2016a). During the initial creep-ageing period, naturally-aged small precipitates and clusters dissolve, and T_1 and θ' precipitate nucleation is widespread and rapid afterwards because of existing dislocations in the pre-stretched material. New precipitates then grow continuously to the peak-aged state, and over-ageing takes place with further coarsening of T_1 and S precipitates.

The double primary creep feature was reported to be mainly controlled by microstructural evolution, including dislocations, solutes and precipitates (Li et al., 2016a). Similar to conventional creep mechanisms, dislocation hardening plays a dominant role during initial primary and transient steady creep stages (Fig. 1). The fast depletion of solutes because of accelerated nucleation of T_1 and θ' precipitates contributes to a decrease of creep resistance for the alloy, leading to the subsequent intermediate inverse creep stage with increasing creep strain rate. As ageing continues, the growth of precipitates contributes more to the hardening of the material, resulting in a second primary creep stage. The creep strain rate decreases until it reaches a stable level at the second steady stage.

3. Microstructural examination of creep-aged Al-Cu-Li alloy

Quantitative TEM and related SAXS analysis have been carried out to examine the evolution of precipitates during creep-ageing of AA2050-T34. Both the precipitate size and corresponding volume fraction have been measured to facilitate the development and calibration of the constitutive model.

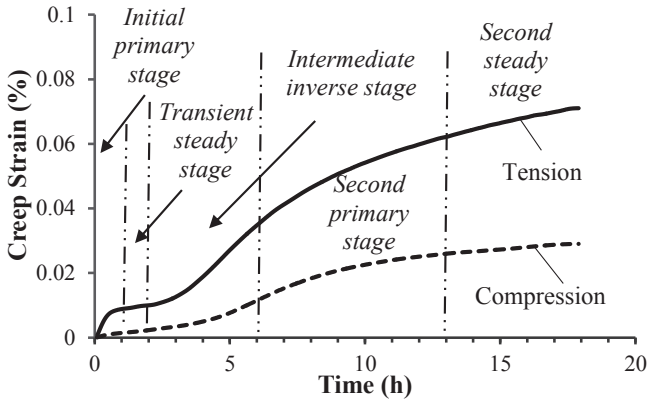

Fig. 1. Asymmetric double primary creep feature during tensile (solid line) and compressive (dashed line) creep-ageing of AA2050-T34 under 150 MPa at 155 °C.

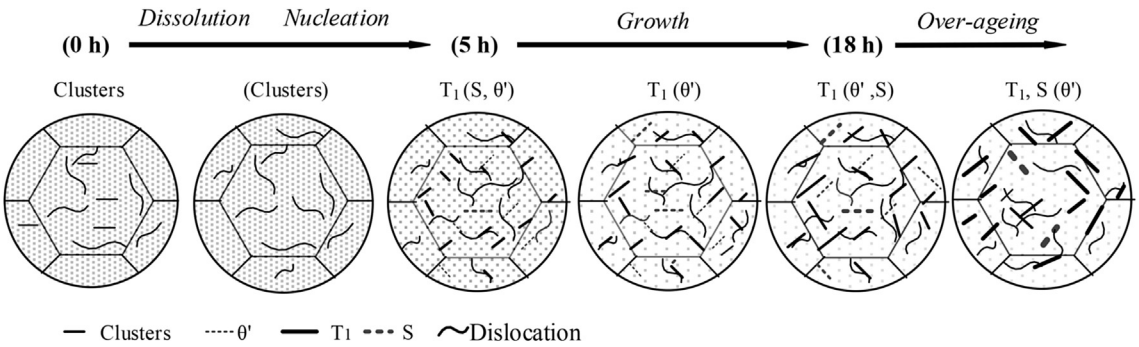

Fig. 2. Schematic showing evolution of microstructures during creep-ageing of AA2050-T34.

TEM observations were made for selected specimens: the as-received material, and 5, 10 and 18 h tension creep-aged specimens under 150 MPa. The TEM specimens were prepared by cutting 3 mm diameter discs along the stress direction, thinning the discs mechanically to 0.08 mm afterwards and then twin-jet-electropolishing them to perforation with a mixture of 1/3 nitric acid and 2/3 methanol at −20 °C, using a potential of 10 V. The TEM specimens were then examined using a Tecnai F20 (200 kV) field-emission-gun scanning transmission electron microscope. The SAXS samples were sliced from the same position as that of TEM samples and ground to thin plates with 6×6 cm^2 in area and 60–70 μm in thickness. The SAXS experiments were carried out on a BRUKER AXS GmbH NANOSTAR working with a Cu Kα source. The beam size was

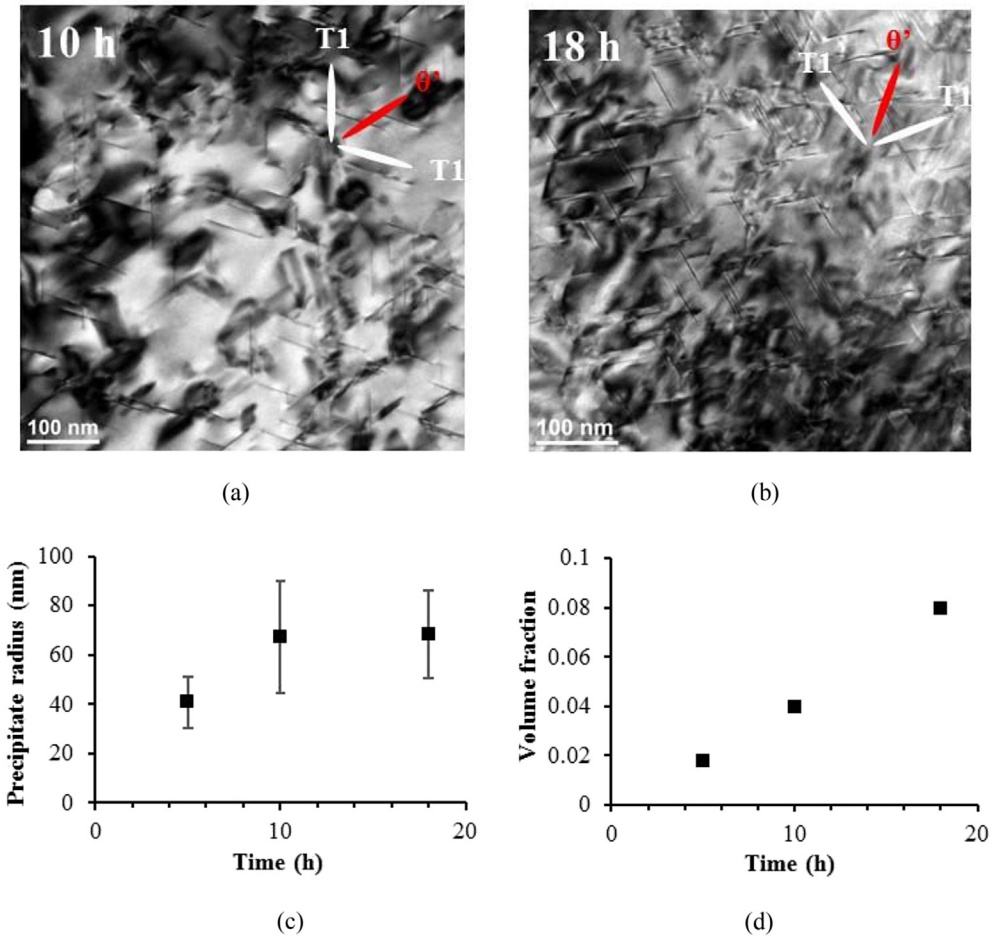

Fig. 3. Selected TEM images of (a) 10 h and (b) 18 h creep-aged samples; (c) T_1 precipitate radius and (d) volume fraction data of the 5, 10 and 18 h creep-aged samples.

approximately 0.4 mm in diameter and the collection time was 1.5 h to allow for sufficient intensity of scattering from precipitates in the samples.

Fig. 3(a) and (b) show TEM observations of the distributions of T_1 and θ' precipitates in 10 and 18 h creep-aged samples along the [110] zone axis of the fcc matrix. The different precipitates can be distinguished according to the corresponding orientation relationships of T_1 and θ' with respect to the matrix in the creep-aged samples (Fig. 3(a) and (b)), also demonstrated in an earlier study (Li et al., 2016a). The ratio of T_1 to θ' precipitates has been experimentally measured as approximately 25–30 to 1 in all examined samples, indicating that T_1 plays the dominant role in strengthening the alloy during creep-ageing. Hence, θ' precipitates may be neglected in the current study for modelling the creep-ageing behaviour of the alloy.

The radius data of T_1 precipitates is presented in Fig. 3(c), showing a continuously growing trend during 18 h creep-ageing. Each data point with its corresponding standard deviation was obtained from the measurement of 50 precipitates of T_1 phase in each TEM sample. In order to quantify the volume fraction of T_1 phase, it is necessary to utilise the SAXS technique (rather than TEM) for the following reason. There are four variants of the T_1 phase, which has {111} habit planes. Under TEM observation along the [110] zone axis of the Al matrix, two variants of the T_1 phase are in the edge-on configuration, but the other two variants are not. The latter variants are inclined to the [110] zone axis, and possibly located above or below each other, which results in overlapping in the two-dimensional TEM image, which makes measurement of the T_1 precipitate density difficult. On the contrary, the intensity of SAXS from T_1 precipitates is proportional to its volume fraction. Methods of estimation of the volume fraction of T_1 phase are discussed in (Donnadieu et al., 2011), and the method used in the SAXS analysis in this study to obtain the volume fraction of T_1 precipitates is explained in the Supplementary Material. The data are plotted in Fig. 3(d), showing a continuously increasing volume fraction during the entire creep-ageing process.

4. Model development

The unified model developed in this study is based on an internal microstructural variable approach, in which relationships between material properties and corresponding microstructural variables are considered. All equations in the model were developed in their rate forms, so as to represent the evolutionary nature of related material properties during the CAF process (Lin and Dean, 2005). For age hardening during the CAF process, the yield strength (σ_y) of the alloy is determined by precipitation (σ_p), solid solution (σ_{ss}) and dislocation (σ_{dis}) hardening. All these strength components are affected by relevant microstructural variables (Shercliff and Ashby, 1990), as shown in Eq. (1). Similarly, the creep strain (ε_{cr}) during the CAF process is determined by not only the applied stress ($\overline{\rho}$), but also the corresponding microstructural variables (Eq. (2)) (Kowalewski et al., 1994; Li et al., 2016a):

$$\sigma_y = f\left(\sigma_p, \sigma_{ss}, \sigma_{dis}\right) = F(r, c, \rho) \tag{1}$$

$$\varepsilon_{cr} = f(\sigma, r, c, \rho) \tag{2}$$

where r, c and ρ are respectively the precipitate radius, solute concentration in the matrix and dislocation density in the material.

The evolution of these microstructural variables during the CAF process will be analysed and modelled in Section 4.1. By relating these variables to corresponding properties of the alloy during the CAF process, the age hardening and creep deformation of the alloy will be evaluated and modelled respectively in Sections 4.2 and 4.3.

4.1. Evolution of internal microstructure variables

4.1.1. Dislocation density

The evolution of dislocation density during plastic deformation is determined by dislocation storage and dynamic recovery effects, which have been modelled in many previous publications (Kocks, 1976; Li et al., 2009). Its rate form can be derived as:

$$\dot{\rho} = K_1\sqrt{\rho}\dot{\varepsilon}_{cr} - K_2\rho(\dot{\varepsilon}_{cr})^N \tag{3}$$

where K_1, K_2 and N are constants. The first term on the right-hand side of Eq. (3) characterises dislocation accumulation and the second term represents dislocation annihilation by dynamic recovery. A normalised dislocation density $\overline{\rho}$ is used in this study (Zhan et al., 2011b):

$$\overline{\rho} = \frac{\rho - \rho_i}{\rho_s} \tag{4}$$

where ρ_s is the saturated dislocation density and ρ_i is the dislocation density of the alloy in its initial state. An assumption that $\rho_i \ll \rho_s$ is used here to simplify the model, hence $\overline{\rho}$ varies from 0 (initial) to 1 (saturated) during the CAF process. It is believed

that the saturation of the dislocation density appears after the primary creep stage. When the dislocation density reaches its saturate level, $\bar{\rho}$ tends to 1 and $\dot{\bar{\rho}}$ tends to be zero (Zhan et al., 2011b). Therefore, Eq. (3) can be adapted to the following format:

$$\dot{\bar{\rho}} = A_1(1-\bar{\rho})|\dot{\varepsilon}_{cr}|^{m_1} \tag{5}$$

where A_1 and m_1 are material constants to replace the corresponding constants K_1, K_2 and N in Eq. (3). In addition, since the CAF process is carried out at an elevated temperature, static recovery can also play a role in the dislocation evolution. As a result, Eq. (5) is amended by adding a static recovery term (Lin and Liu, 2003):

$$\dot{\bar{\rho}} = A_1(1-\bar{\rho})|\dot{\varepsilon}_{cr}|^{m_1} - C_p\bar{\rho}^{m_2} \tag{6}$$

where C_p and m_2 are material constants.

4.1.2. Precipitate radius

As shown in Section 3, T_1 is the main strengthening precipitate in AA2050-T34 during creep-ageing. This phase is disc-shaped with large aspect ratio (Cassada et al., 1991) and its dimensions (radius r and thickness h) are schematically shown in Fig. 4(a). The aspect ratio (A) can be assumed to be a fixed value during its growth (Li et al., 2010) and therefore the precipitate radius (r) is used to represent the evolution of T_1 phase in this study.

According to earlier studies (Kumar et al., 1996; Li et al., 2016a), naturally-aged precipitates will dissolve during the initial stage of CAF of AA2050-T34, resulting in the initial lowering of yield strength. On the other hand, new precipitates will nucleate and strengthen the alloy, as discussed earlier. Hence, the evolution of both the dissolving and new precipitate radius (r_d and r_n respectively), as schematically shown in Fig. 4(b), will be considered in the model.

Precipitation is a common phenomenon in artificial ageing of aluminium alloys and has been widely investigated. It has been reported that pre-stretched Al-Cu-Li alloys experience significantly accelerated nucleation of precipitates at the initial stage of artificial ageing compared with un-deformed alloys, because of high energy sites provided by existing dislocations (Kumar et al., 1996). Growth of precipitates then takes place with only minor new nucleation (Cassada et al., 1991; Decreus et al., 2013), making it similar to coarsening with saturated nucleation of precipitates (Shercliff and Ashby, 1990). Hence, in this study the well-known cubic coarsening law (Lifshitz and Slyozov, 1961) is used to approximate the evolution of precipitate radius (r_n) during creep-ageing of AA2050-T34:

$$r_n^3 - r_{n_0}^3 = \frac{c_1 t}{T}\exp\left(-\frac{Q_A}{RT}\right) \tag{7}$$

where c_1 is a kinetic factor and Q_A is the activation energy for diffusion. For the isothermal CAF process, both coefficients can be treated as constants. R is the universal gas constant and T is the temperature in Kelvin which can also be treated as a constant in the CAF process.

A normalised precipitate radius is introduced as below:

$$\bar{r}_n = \frac{r_n}{r_c} \tag{8}$$

where r_c is the precipitate radius at the peak-ageing state of the material. Thus $\bar{r}_n < 1$ represents under-ageing states and $\bar{r}_n > 1$ indicates over-ageing conditions. Eq. (7) can then be transformed into a rate evolution form of the normalised precipitate radius:

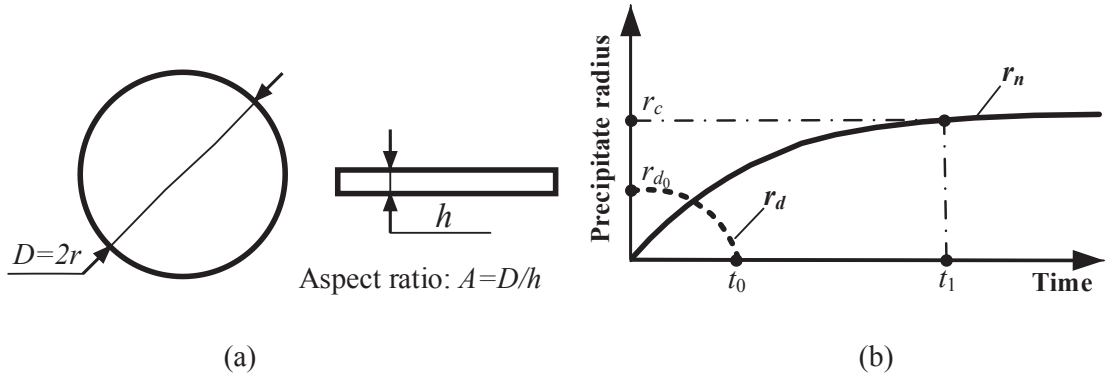

Fig. 4. Schematics showing (a) a disc-shaped precipitate and (b) the size evolution of the dissolving (r_d) and new precipitates (r_n) during creep-ageing of AA2050-T34.

$$\dot{\bar{r}}_n = \frac{1}{3r_c^3}\frac{c_1}{T}\exp\left(-\frac{Q_A}{RT}\right)\frac{1}{\bar{r}_n^2} = \frac{K}{\bar{r}_n^2} \tag{9}$$

where K is a temperature-dependent constant. In order to eliminate possible numerical difficulties near $\bar{r}_n = 0$, Eq. (9) is transformed to a new form while keeping its main characteristics:

$$\dot{\bar{r}}_n = C_r(Q - \bar{r}_n)^{m_3} \tag{10}$$

where Q represents the saturation state of precipitate growth and C_r and m_3 are constants, which control the growth speed of precipitates. The detailed mathematical transformation process is presented in the Appendix.

During creep-ageing, the precipitation progress is also affected by the dislocations generated by creep deformation, which will accelerate the precipitation growth (Lin et al., 2006). A dislocation density controlling component is added to Eq. (10) to take into account this effect, as follows (Zhan et al. (2011b):

$$\dot{\bar{r}}_n = C_r(Q - \bar{r}_n)^{m_3}(1 + \gamma_0\bar{\rho}^{m_4}) \tag{11}$$

where γ_0 and m_4 are material constants.

Similarly, a normalised radius is introduced for the dissolving precipitates:

$$\bar{r}_d = \frac{r_d}{r_{d_0}}. \tag{12}$$

where r_{d_0} is the initial value of the dissolving precipitate radius. $\bar{r}_d$ will then vary from 1 to 0 during the CAF process of AA2050-T34.

The dissolution kinetics of precipitates during ageing have been summarised as (Aaron and Kotler, 1971; Thomas and Whelan, 1961; Whelan, 1969):

$$\dot{\bar{r}}_d = -\frac{\eta}{2}\left(\frac{D}{\pi t}\right)^{1/2} - \frac{\eta D}{2\bar{r}_d} \tag{13}$$

where η is a constant and D is the coefficient of diffusion. The first term $(-\eta(D/\pi t)^{1/2}/2)$ plays a dominant role in initial dissolution when the diameter of precipitates is large, leading to a decreasing rate with time. When the precipitate diameter is small (e.g. $r < 2000$ Å for some Al-Cu alloys indicated by (Thomas and Whelan, 1961)), after very short transient time the second term $(-\eta D/2\bar{r}_d)$ becomes large compared with the first term, and controls the dissolution process. As the naturally-aged precipitates in Al-Cu-Li alloys are very small, of the order of 20 Å (Decreus et al., 2013), their dissolution progress during creep-ageing can be approximated by only considering the dominant effects from the second term in Eq. (13), as:

$$\dot{\bar{r}}_d = -\frac{\eta D}{2\bar{r}_d} = -\frac{C_{r1}}{\bar{r}_d} \tag{14}$$

where material constant C_{r1} replaces the coefficients η and D.

4.1.3. Solute concentration

The equilibrium solute concentration (c_e) in the matrix depends on temperature. The solute concentration reaches its saturation value after solution heat treatment and will then decrease towards an equilibrium value for the ageing temperature in subsequent ageing because of precipitation. Its evolution has been investigated and modelled previously (Wu and Ferguson, 2009) and the resultant rate equation can be written as:

$$\dot{c} = -A_2(c - c_a) \tag{15}$$

where A_2 is a material constant and c_a is the equilibrium solute concentration at the ageing temperature. Normalised solute concentration is defined as:

$$\bar{c} = \frac{c}{c_s} \tag{16}$$

where c_s is the equilibrium solute concentration of the alloy at its SHT temperature. $\bar{c}$ will then vary from approximately 1 to $\bar{c}_a$ during ageing of an as-quenched alloy, where $\bar{c}_a = c_a/c_s$ is the normalised solute concentration at the ageing temperature. For AA2050-T34, the loss of solutes has already taken place because of natural ageing, hence its initial normalised value in creep-ageing is no longer 1 and will be determined in Section 5 below. In addition, although the dissolving precipitates may lead to a slight increase of solute concentration in the matrix in the initial stage of creep-ageing, the effect is ignored here as

this slight increase is much smaller than the significant solute loss due to precipitation during subsequent creep-ageing and is expected to contribute little to the resultant creep-ageing behaviour.

Similar to the evolution of precipitates, creep deformation also affects the solute loss during the CAF process. As the growth of precipitates can be treated as directly proportional to the solute loss (Shercliff and Ashby, 1990), the same dislocation density term from Eq. (11) is introduced into Eq. (15). In addition, by replacing the solute concentration variables with their normalised values, Eq. (15) can be modified as:

$$\dot{\bar{c}} = -A_2(\bar{c} - \bar{c}_a)(1 + \gamma_0 \bar{\rho}^{m_4}) \tag{17}$$

4.2. Age hardening phenomenon during the CAF process

The strengthening phenomenon of the alloy during the CAF process is generally attributed to three strength components, including dislocation, precipitation and solid solution hardening, as shown in Fig. 5. These components are determined by the corresponding internal microstructural variables analysed in Section 4.1 and will be modelled in this section.

4.2.1. Dislocation hardening

Dislocation hardening is a common phenomenon which can be observed in almost all metal forming processes, including the CAF process. Many investigations have been carried out to model this phenomenon according to the evolution of dislocation density (Estrin, 1998; Kocks, 1976). Its rate equation can be summarised as:

$$\dot{\sigma}_{dis} = A_3 n \bar{\rho}^{n-1} \dot{\bar{\rho}} \tag{18}$$

Where A_3 and n are material constants.

4.2.2. Precipitation hardening

As discussed in Section 4.1.2, both dissolution of existing precipitates and nucleation of new precipitates occur during creep-ageing of AA2050-T34. Their contributions to precipitation hardening of the material are analysed separately.

For the new precipitates, Shercliff and Ashby (1990) have proposed a set of equations to describe their contributions to the strength during the artificial ageing process, in which microstructural variables of precipitate radius (r_n) and volume fraction (f) were used. The precipitation hardening is assumed to be mainly controlled by strengthening from shearable precipitates (shearing strength, σ_A) before peak-ageing and nonshearable precipitates (bypassing strength, σ_B) in over-ageing, as shown in Fig. 5, which have been modelled separately (Kelly and Nicholson, 1963):

$$\begin{aligned} \sigma_A &= c_1 f^{m_a} r_n^{n_a} \\ \sigma_B &= c_2 f^{m_b} / r_n^{n_b} \end{aligned} \tag{19}$$

where c_1 and c_2 are material constants including contributions from precipitates with fixed aspect ratio (A), and m_a, m_b, n_a and n_b are coefficients to determine the strengthening contributions from the volume fraction and radius of precipitates.

Considering the significant nucleation of precipitates in the initial stage of artificial ageing of AA2050-T34, as discussed earlier, it is reasonable to assume that growth of the precipitates with only slight further nucleation occurs over the greater

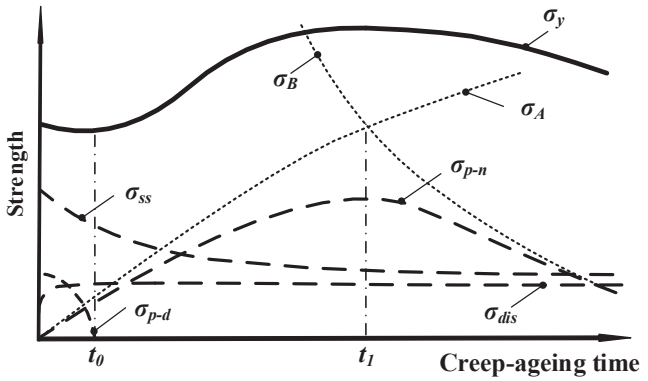

Fig. 5. A schematic diagram of the yield strength evolution during creep-ageing of AA2050-T34 and the contributions from solid solution hardening (σ_{SS}), dislocation hardening (σ_{dis}) and precipitation hardening (comprising of dissolving precipitates (σ_{p-d}), shearable (σ_A) and nonshearable (σ_B) new precipitates (σ_{p-n})).

part of the growth stage during creep-ageing (Starink and Wang, 2003). Therefore, the relationship between relative volume fraction (f_r) and precipitate radius may be approximated through a cell assumption as proposed by Reti and Flemings (1972):

$$f_r = \frac{f}{f_c} = \left(\frac{r_n}{r_c}\right)^3 \tag{20}$$

where f_c is the saturated volume fraction of precipitates. Fig. 6 compares the relationship according to Eq. (20) with the experimental data from Section 3, where data at 18 h are treated as r_c and f_c. Fig. 6 shows that Eq. (20) is a fair representation of the relationship between the relative volume fraction and the normalised precipitate radius for the alloy.

During over-ageing, the volume fraction of precipitates reaches its saturation level and the corresponding relative volume fraction can be regarded as 1. Substituting f in Eq. (19) with f_r and using the normalised $\bar{r}_n$ to replace r_n, the precipitation hardening equation can be written as:

$$\begin{aligned} \sigma_A &= c_1\left(\frac{f_c}{r_c^3}\right)^{m_a} r_n^{3m_a+n_a} = c_1' \bar{r}_n^{n_1} \\ \sigma_B &= \frac{c_2}{r_n^{n_b}} = \frac{c_2'}{\bar{r}_n^{n_2}} \end{aligned} \tag{21}$$

where c_1' and c_2' are used to replace all the other constants, such as c_1, c_2, f_c and r_c; n_1 and n_2 replace the exponents m_a, n_a and n_b. Since the evolution (hardening) of σ_A (see Fig. 5) is monotonically increasing *and* convex with respect to $\bar{r}_n$, its gradient, $d\sigma_A/d\bar{r}_n = c_1' n_1 \bar{r}_n^{n_1-1}$, should be a monotonically decreasing function of $\bar{r}_n$ (Abbena et al., 2006), hence the material constant n_1 must be in the range $0 < n_1 < 1$.

The dominant strengthening mechanism of precipitates will change from shearing to bypassing when peak-ageing of the alloy occurs ($\sigma_A = \sigma_B$) as shown in Fig. 5. The overall precipitation strength (σ_{p-n}) is mathematically approximated by the harmonic mean, as described in (Shercliff and Ashby, 1990):

$$\sigma_{p-n} = \left(\frac{1}{\sigma_A} + \frac{1}{\sigma_B}\right)^{-1} = \frac{\sigma_A \sigma_B}{\sigma_A + \sigma_B} \tag{22}$$

Considering the mathematical boundary conditions of this harmonic mean precipitation hardening model, when peak-ageing occurs ($\bar{r}_n = 1$) the shearing strength should be equal to the bypassing strength ($\sigma_A = \sigma_B$). As a result, it can be deduced that $c_1' = c_2' = c$. Moreover, considering the basic property of the harmonic mean function, when $\bar{r}_n = 1$, the precipitation strength reaches its peak state and its corresponding rate should then be zero ($\dot{\sigma}_{p-n} = 0$). Consequently, n_1 will equal n_2 ($n_1 = n_2 = n$). The rate equation for the overall yield strength resulting from newly nucleated precipitates becomes:

$$\dot{\sigma}_{p-n} = \frac{cn\dot{\bar{r}}_n\left(1 - (\bar{r}_n)^{2n}\right)}{\left((\bar{r}_n)^{2n} + 1\right)^2 (\bar{r}_n)^{1-n}} \tag{23}$$

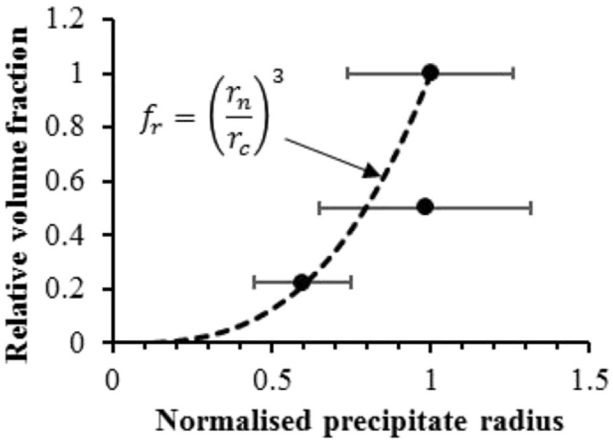

Fig. 6. Comparison of experimental data and Eq. (20) relating relative volume fraction to normalised radius of T_1 precipitates during creep-ageing of AA2050-T34.

Using a similar mathematical technique to that used for the precipitate radius equations (Eqs. (9) and (10); see Appendix), the denominator in Eq. (23) is converted into a numerator to avoid potential numerical difficulties in evaluating the equation:

$$\dot{\sigma}_{p-n} = cn\dot{\bar{r}}_n\left(1-(\bar{r}_n)^{2n}\right)c'(Q-\bar{r}_n)^{n'} \tag{24}$$

Now consider the rate equation for precipitate radius (Eq. (10)) (ignoring creep deformation effects), the above equation can be converted into the following:

$$\dot{\sigma}_{p-n} = C_a\dot{\bar{r}}_n^{m_5}\left(1-\bar{r}_n^{m_6}\right) \tag{25}$$

where C_a, m_5 and m_6 are material constants.

For the dissolving precipitates during creep-ageing of AA2050-T34, the precipitates from natural ageing are much less developed than their peak-aged counterparts. Therefore the shearing mechanism should play the dominant role in the precipitate strengthening, and this contribution to the yield strength can be modelled using the shearing strength model given by Eq. (21) as:

$$\dot{\sigma}_{p-d} = C_{a1}\bar{r}_d^{m_7}\dot{\bar{r}}_d \tag{26}$$

where C_{a1} and m_7 are material constants.

The overall precipitation strength from both dissolving precipitates and new precipitates can be modelled by a classical law of mixtures (Kocks et al., 1975):

$$\sigma_p = \left(\sigma_{p-d}^2+\sigma_{p-n}^2\right)^{1/2} \tag{27}$$

4.2.3. Solid solution hardening

The solid solution hardening of the material is determined by the solute concentration in the matrix and the rate of this strength component can be modelled as (Wu and Ferguson, 2009):

$$\dot{\sigma}_{ss} = -c_3\frac{(\bar{c}-\bar{c}_a)}{\left(c_4-\dot{\bar{c}}\right)^{1-m}} \tag{28}$$

where c_3, c_4 and m are material constants and m is generally set equal to 2/3 (Wu and Ferguson, 2009). Using the same mathematical approximation method utilised for Eqs. (9) and (23), the above equation can be simplified as:

$$\dot{\sigma}_{ss} = -C_{SS}\left|\dot{\bar{c}}\right|^{m_8}(\bar{c}-\bar{c}_a) \tag{29}$$

where C_{SS} and m_8 are material constants.

4.2.4. Overall yield strength

The overall yield strength of the alloy during the CAF process can be modelled according to a classic law of mixtures to include all three strengthening components: precipitation hardening, dislocation hardening and solid solution hardening (including the intrinsic strength of aluminium) (Kocks et al., 1975):

$$\sigma_y = \sigma_{ss}+\sqrt{\sigma_{dis}^2+\sigma_p^2} \tag{30}$$

4.3. Creep deformation behaviour during the CAF process

The creep behaviour of AA2050-T34 during the CAF process, which has been studied previously (Li et al., 2016a), demonstrates a new double primary creep feature with five creep stages. In this study, a widely used creep strain rate model with a hyperbolic function (Kowalewski et al., 1994; Othman et al., 1993) has been adapted and modified based on creep-ageing properties of AA2050-T34. As introduced in Section 2 and discussed in detail in an earlier study (Li et al., 2016a), the creep behaviour of AA2050-T34 during the CAF process is different from the conventional two-stage creep behaviour which can be explained by effects from dislocation hardening and recovery (Mitra and McLean, 1966). The evolution of the three microstructural parameters, namely dislocation density, solute concentration and precipitate radius all contribute to the new double primary creep feature of the alloy. In order to consider these effects, a microstructure-controlled creep variable H is introduced in the creep strain rate equation, as follows:

$$\dot{\varepsilon}_{cr} = A_4 \sinh\{B_1 \sigma_{ea}(1-H))\} sign(\sigma) \tag{31}$$

$$H = k_1 \overline{\rho} + k_2 \overline{c} + k_3 \left(\overline{r}_n + \beta^{1/2} \overline{r}_d \right) \tag{32}$$

$$\sigma_{ea} = \sigma - \sigma_{th_0} \tag{33}$$

where A_4 and B_1 are material constants. The creep variable H was determined by three controlling microstructural variables – normalised dislocation density ($\overline{\rho}$), solute concentration ($\overline{c}$) and precipitate radius ($\overline{r}$); k_1, k_2 and k_3 are weighting factors ranging from 0 to 1 to control the relative effects of $\overline{\rho}$, $\overline{c}$, $\overline{r}_n$ and $\overline{r}_d$ on the creep behaviour of the alloy. A coefficient β was introduced to account for differing contributions from dissolving and new precipitates ($\overline{r}_d$ and $\overline{r}_n$). In order to characterise the creep resistance of the as-received material, in which both initial dislocations and precipitates are present, a threshold stress (σ_{th}) was introduced for the alloy and is defined as the stress below which creep rates can be negligible (Seidman et al., 2002; Sherby and Burke, 1968). To model this effect, an effective applied stress (σ_{ea}) is introduced into the above model (Li et al., 2010), which is calculated as the applied stress (σ) minus the initial threshold stress of the material before creep-ageing tests (σ_{th_0}) in Eq. (32).

Varying properties of microstructural variables under different stress directions, such as the inverse precipitate orientations, which result in different creep resistances of the alloys, play an important role in the asymmetric tension and compression creep-ageing behaviour of AA2050-T34 (Li et al., 2016a). Their different contributions to tension and compression creep behaviour can be captured by varying the weighting factors k_1, k_2 and k_3, as well as the resultant threshold stress σ_{th_0} in the equations. Hence, the same set of constitutive equations proposed above can be used in both tension and compression creep-ageing conditions to predict the asymmetric creep-ageing behaviour of the alloy by simply re-calibrating the creep resistance related material constants (B_1, σ_{th_0}, k_1, k_2, k_3) in the model.

5. Model implementation

5.1. Estimation of initial and equilibrium states of internal variables

5.1.1. Initial strength components

The initial overall yield strength of AA2050-T34 comprises of three contributions from solid solution strengthening (σ_{SS_0}), dislocations (σ_{dis_0}) from pre-stretching and naturally-aged precipitates (σ_{p-d_0}). The strength from new precipitates (σ_{p-n_0}) is 0. The number of solutes diffusing from the matrix to precipitates after natural ageing is much smaller than that after artificial ageing and thus the slight reduction of the initial solution strength during natural ageing will be ignored here. Consequently, σ_{SS_0} can be estimated by the yield strength of the solution heat treated alloy (σ_{y1} in Fig. 7). On the other hand, σ_{dis_0} can be calculated from the yield strength of the solution heat treated, water quenched and pre-stretched alloy (σ_{y2}), as shown in Fig. 7. Finally, σ_{p-d_0} can be approximately determined by Eq. (30). The heat treatment process of the alloy and related calculations are demonstrated in Fig. 7 and detailed results are listed in Table 1.

The initial threshold stress of the as-received material (σ_{th_0}) can be determined by using the power-law creep equation (Seidman et al., 2002). For AA2050-T34, the corresponding creep resistance of the material in both tension and compression

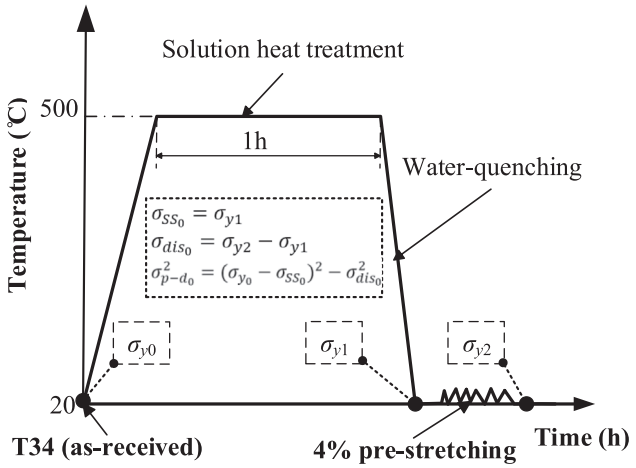

Fig. 7. Schematic of heat treatment process and calculations to determine initial strength components of AA2050-T34.

Table 1
Estimated initial and equilibrium values of variables for AA2050-T34 at 155 °C.

Initial value									Equilibrium value
$\bar{\rho}_0$	$\bar{c}_0$	$\bar{r}_{d_0}$	$\bar{r}_{n_0}$	β	σ_{p-d_0} (MPa)	σ_{p-n_0} (MPa)	σ_{SS_0} (MPa)	σ_{dis_0} (MPa)	$\bar{c}_a$
1E-5	0.978	1	0	0.318	110	0	120	100	0.316

creep-ageing conditions has been investigated in detail (Li et al., 2016b), in which the initial tension threshold stress was obtained as 18 MPa and the initial compression threshold stress was 58 MPa for AA2050-T34 (as listed in Table 3).

5.1.2. Equilibrium solute concentration

The relationship between the equilibrium solute concentration (c_e) and the temperature in Al-Li alloys can be calculated according to the following general equation (Prasad and Ramachandran, 2014):

$$\ln c_e(at.\%) = 4.176 - \frac{9180\ (J/mol)}{RT} \tag{34}$$

Hence, the normalised equilibrium solute concentration at the creep-ageing temperature ($\bar{c}_a = c_a/c_s$) can be obtained (as listed in Table 1), in which c_a and c_s are the equilibrium solute concentrations at the creep-ageing temperature (155 °C) and at the SHT temperature (500 °C), respectively, and can be obtained by Eq. (34).

5.1.3. Initial normalised precipitate radius and solute concentration

Although the normalised precipitate radii $\bar{r}_d$ and $\bar{r}_n$ will both be 1 at their maximum strength states, their contributions to strength and creep are different. The dissolving precipitates ($\bar{r}_d$) are considered to be equivalent to $\bar{r}_n$ by multiplying by a coefficient $\beta^{1/2}$ in Eq. (32). The coefficient can be estimated according to their strength contributions. As both precipitates in the alloy develop before the peak-ageing state is achieved in this study, the shearing mechanism has been used to approximate their strength contributions, as demonstrated in Eqs. (19) and (20), where the constants m_a and n_a are set to 0.5 (Starke Jr., 1977). The maximum strength contributions from dissolving precipitates and new precipitates can be approximated as σ_{p-} and σ_{p+} respectively from the yield strength curve during the CAF process, as schematically shown in Fig. 8. Thus β can be estimated as:

$$\frac{\sigma_{p-}}{\sigma_{p+}} = \left(\frac{\beta^{1/2}\bar{r}_{d_0}}{\bar{r}_c}\right)^2 = \beta \tag{35}$$

In addition, the normalised solute concentration can be related to the relative volume fraction of precipitates (Esmaeili et al., 2003a; Shercliff and Ashby, 1990), which can also be expressed as a function of normalised precipitate radius according to Eq. (20):

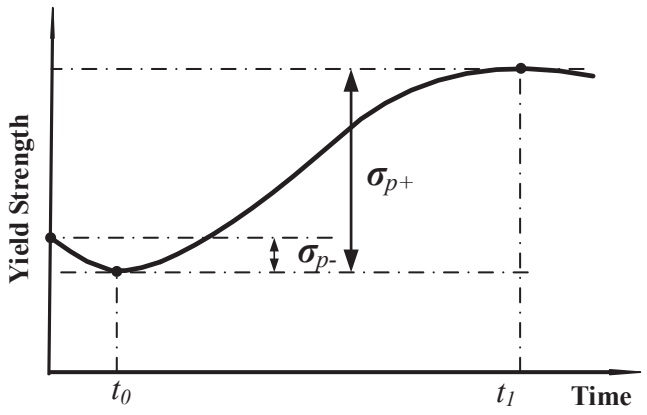

Fig. 8. A schematic depiction of strength reversion (σ_{p-}) from dissolving precipitates, and strengthening from new precipitates (σ_{p+}) during the CAF of AA2050-T34.

$$\bar{c} = 1 - \alpha f_r = 1 - \alpha\left(\frac{r_n}{r_c}\right)^3 = 1 - \alpha\bar{r}_n^3 \tag{36}$$

At the peak-ageing state, $\bar{r}_n = \bar{r}_c = 1$ and $\bar{c}_a = 0.316$, thus the coefficient α is 0.684 for AA2050-T34. Consequently, the initial normalised solute concentration ($\bar{c}_0$) of the alloy can be estimated according to Eq. (36) by the equivalent initial normalised precipitate radius ($\bar{r}_n = \beta^{1/2}\bar{r}_{d_0}$). The initial values of these variables are listed in Table 1.

5.2. Determination of material constants

The proposed set of constitutive equations for the CAF process, including those for the evolution of microstructural variables (Eqs. (6), (11), (14) and (17)), yield strength (Eqs. (18), (25), (26), (29) and (30)) and creep strain (Eq. (31)), are non-linear ordinary differential equations, which cannot be solved analytically. In order to determine the unknown material constants in the whole model, a combined numerical-manual method has been used. A numerical optimisation technique (Li et al., 2002; Lin and Yang, 1999) was used first to obtain an initial set of constants and a manual multi-step fitting process (Zhan et al., 2011b) was applied afterwards to fine tune the initial constants, achieving good agreement between experiments and simulations.

Firstly, a numerical optimisation technique to obtain the minimum sum of the squares of the errors between the experimental and numerical data has been applied for initial tensile creep-ageing related material constants determination. The objective function is defined by experimental and numerical differences of creep strain at the same time and stress conditions, as follows (Lin and Yang, 1999):

$$f(x) = \sum_{j=1}^{n_1}\sum_{i=1}^{m_j} w_{ij}\left(\varepsilon_{ij}^c - \varepsilon_{ij}^e\right)^2 \tag{37}$$

where x ($x = (x_1, x_2, \ldots, x_s)$) is the material constant and s is the number of constants to be optimised; n_1 is the number of creep curves in the experiments, m_j is the number of experimental data points for the jth creep curve, i and j represent the ith experimental data for the jth creep curve respectively, w_{ij} is a weighting function and $(\varepsilon_{ij}^c - \varepsilon_{ij}^e)$ is the difference between the computed and experimental creep strain results corresponding to the same time.

The numerical procedure was followed by a manual multi-step fitting method to finely adjust the constants and determine the stress direction related constants for compression conditions according to the corresponding experimental data, which involved the following steps:

(1) Adjust material constants in equations for microstructural variables (Eqs. (11), (14) and (17)) according to precipitate radius data.
(2) Adjust material constants in yield strength related equations (Eqs. (25), (26) and (29)) according to the yield strength curve and the microstructural variables obtained in the previous step.
(3) Consider tension creep strain curves, adjust related material constants (including γ_0 and m_4) in creep strain rate equations (Eqs. (31) and (32)) and creep strain induced dislocation equations (Eqs. (6) and (18)) until good fitting is obtained for all experimental curves under all tested stress levels.
(4) Finally, change creep resistance related material constants in the creep strain rate equations (Eqs. (31) and (32)) to fit compression creep strain curves under different stress levels. The determined material constants for the CAF process of AA2050-T34 are listed in Tables 2 and 3, while corresponding fitting results are shown in Figs. 9–13.

6. Model validation and discussion

6.1. Microstructural evolution

The evolutions of microstructural variables during creep-ageing of AA2050-T34 under a tensile stress of 150 MPa were predicted according to the determined material constants, as shown in Fig. 9. The initial precipitates ($\bar{r}_d$) from natural ageing of the alloy dissolve first and disappear at about 3 h of creep-ageing time, where the lowest yield strength occurs (Li et al., 2016a), as shown in Fig. 9(a). The normalised new precipitate radius ($\bar{r}_n$) grows to 1 after 18 h creep-ageing time, where

Table 2
Material constants for both tension and compression creep-ageing of AA2050-T34 at 155 °C.

A_1 (h^{-1})	m_1	m_2	C_p	C_r (h^{-1})	Q	m_3	C_{r1} (h^{-1})	γ_0	m_4	A_2
1.7	0.03	2.1	0.07	0.108	1.1	1.25	0.165	0.08	1.28	0.45
A_3	n	C_a (MPa)	m_5	m_6	C_{a1} (MPa)	m_7	C_{ss} (MPa)	m_8	A_4	
12	0.8	180	0.65	5.5	110	0.10	40.0	0.02	4.5E-4	

Table 3
Material constants which differ in tension and compression creep-ageing of AA2050-T34 at 155 °C.

Material constants	B_1 (MPa)	k_1	k_2	k_3	σ_{th_0} (MPa)
Tension	1.32E-2	0.618	0.632	0.226	18
Compression	5.0E-3	0.437	0.755	0.360	58

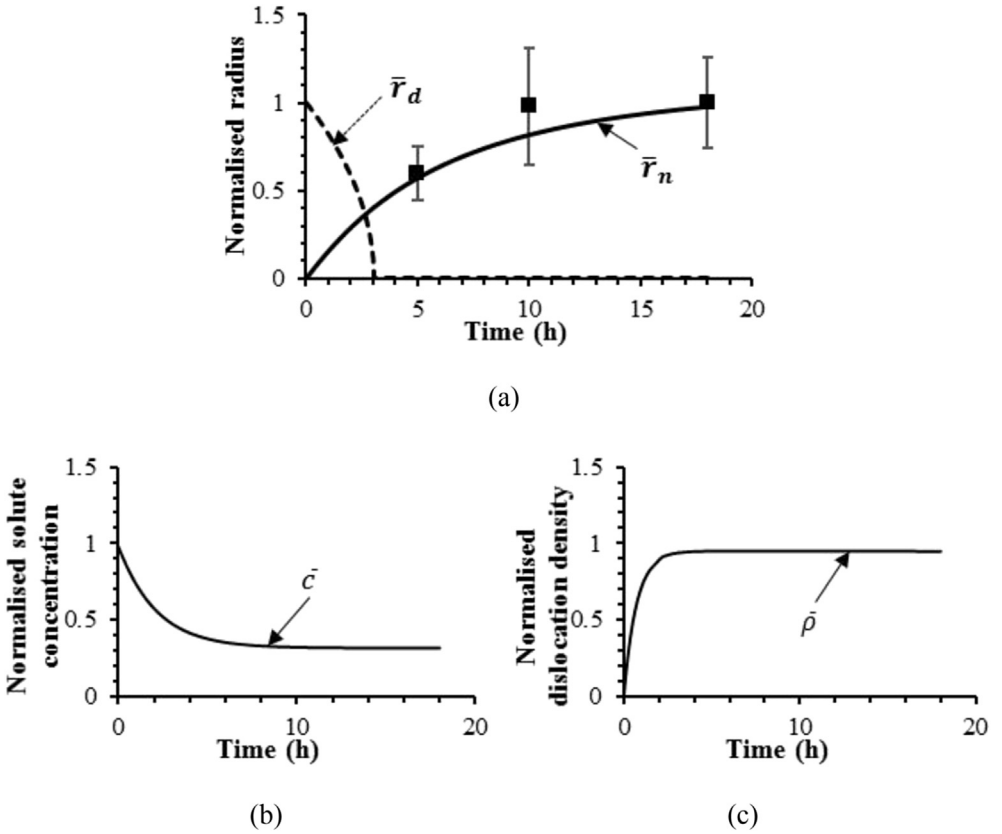

Fig. 9. Predicted evolution of normalised microstructural variables during creep-ageing of AA2050-T34 under 150 MPa at 155 °C: (a) new precipitate radius (solid line, the symbols represent the experimental data) and dissolving precipitate radius (dashed line), (b) solute concentration and (c) dislocation density.

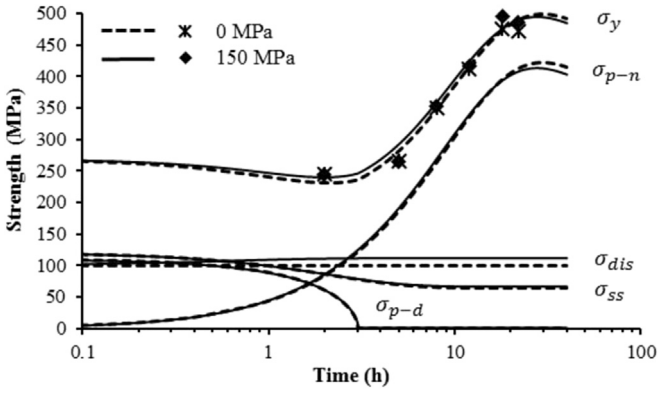

Fig. 10. Comparison of experimental (symbols) (Li et al., 2016a) and predicted hardening behaviour and its strengthening components during pure ageing ($\sigma = 0$ MPa, dashed lines) and creep-ageing ($\sigma = 150$ MPa, solid lines) of AA2050-T34 at 155 °C.

peak-ageing takes place. The experimental data for normalised precipitate radius obtained in Section 3 is also plotted in Fig. 9(a), showing good agreement with the predicted results. The normalised solute concentration ($\bar{c}$) tends to decrease with creep-ageing time (Fig. 9(b)), as the slight compensation of solutes from initial dissolving precipitates has been ignored in the

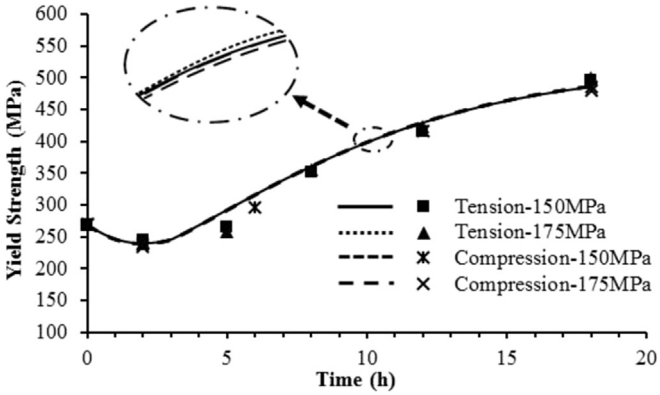

Fig. 11. Comparison of experimental (symbols) (Li et al., 2016a) and predicted (lines) yield strength of AA2050-T34 for tension and compression creep-ageing under 150 and 175 MPa at 155 °C.

model. More apparent decreasing of solute concentration can be observed in the first few hours of creep-ageing time in Fig. 9(b) because the heavily accelerated nucleation of T_1 precipitates occurs at the beginning (Cassada et al., 1991; Li et al., 2016a). The normalised dislocation density ($\overline{\rho}$) plays a dominant role in first two creep stages in the double primary creep feature of AA2050-T34, which lasts about 2 h. It is also predicted to saturate after 2 h of creep-ageing in this model, as shown in Fig. 9(c).

6.2. Yield strength evolution

Fig. 10 compares the numerical results and the experimental data (Li et al., 2016a) for the evolution of overall yield strength (σ_y) and strengthening contributions from new precipitates (σ_{p-n}), dissolving precipitates (σ_{p-d}), dislocations (σ_{dis}) and solid solution (σ_{SS}) of AA2050-T34 under pure-ageing and 150 MPa tensile creep-ageing conditions. The predicted yield strength curves correspond well with the experimental data in both conditions, demonstrating the effectiveness of this new yield strength model and the material constants identified in this study. Both experimental and numerical results show an initial reversion of yield strength in the first 3 h followed by a monotonic increase over the first 18 h of creep-ageing. There is a drop of yield strength between 18 and 22 h of creep-ageing in the experiments, indicating that peak-ageing occurs at around 18 h. While for the numerical results, a fairly comparable peak-ageing time of 24 h was obtained, as the precipitation strengthening mechanism is gradually changed from shearing to bypassing at this stage in the model. Unlike some other 2xxx and 7xxx aluminium alloys during creep-ageing (Lam et al., 2015; Lin et al., 2006; Zhan et al., 2011b), creep-ageing introduces little change in yield strength evolution compared with pure ageing conditions for AA2050-T34, as shown in Fig. 10. This is possibly because precipitation depends heavily on pre-stretching induced dislocations in the as-received material, and that this plays a much more important role in hardening than the dislocations accumulated by creep (Li et al., 2016a). The sensitivity of the effect of creep-induced dislocations on precipitate evolution has been characterised by the material constants γ_0 and m_4 in Eq. (11).

Fig. 11 shows the yield strength evolution of the alloy during creep-ageing under different stress levels and directions (Li et al., 2016a). Because of the dominant precipitation hardening effects during creep-ageing, both stress levels and stress directions have a minor effect on the yield strength evolution. This can be observed in the simulation results in the magnified part of Fig. 11. The insignificant strength difference between the creep-aged samples under 150 and 175 MPa may be expected from the comparison of the results for the 0 and 150 MPa samples in Fig. 10.

6.3. Creep behaviour during creep-ageing

The predicted tension and compression creep strain curves under stress levels from 100 to 187.5 MPa, according to the material constants in Tables 2 and 3, are illustrated in Figs. 12 and 13 respectively. All predicted creep strain curves under either tensile or compressive stresses along the whole creep-ageing time agree well with the experimental results, and the double primary creep feature is well predicted, indicating that the model proposed in this study can successfully predict the asymmetric tension/compression creep strain behaviour during creep-ageing of AA2050-T34. Slight discrepancies between the predicted and experimental creep strain results occur during the first 3 h of creep-ageing time in both Figs. 12 and 13. This discrepancy may be related to the complicated microstructural evolutions at this stage, where dislocations, solid solutes, dissolving and new precipitates will all contribute to the creep strain in complex ways. In the model proposed here, however, the microstructure-controlled creep variable was linearly related to the microstructural variables as in Eq. (32) under both tension and compression conditions. Hence, further research should concentrate more on the detailed effects of these

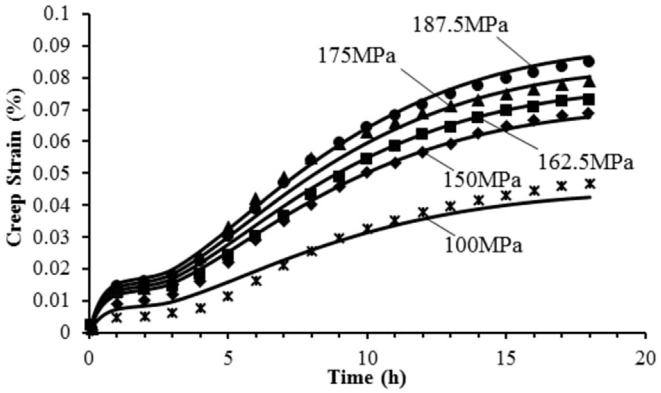

Fig. 12. Comparison of experimental (symbols) (Li et al., 2016a; Li et al., 2016b) and predicted (solid lines) tension creep-ageing curves of AA2050-T34 under different stress levels at 155 °C.

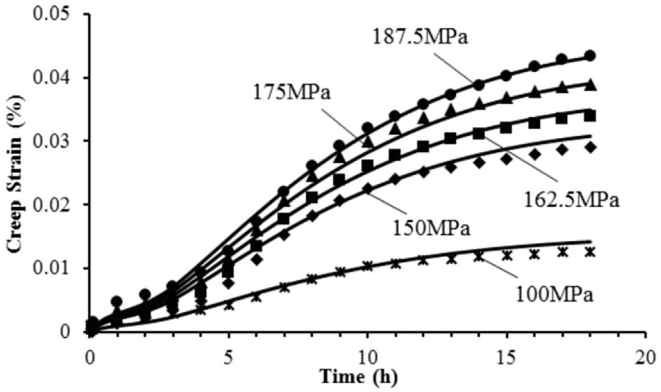

Fig. 13. Comparison of experimental (symbols) (Li et al., 2016a; Li et al., 2016b) and predicted (solid lines) compression creep-ageing curves of AA2050-T34 under different stress levels at 155 °C.

microstructural variables on the creep-ageing behaviour of the alloy at this stage, so as to improve the model and its prediction accuracy in the early stage of creep-ageing.

The model proposed in this study was based on simple physical equations governing materials. Mathematical transformation techniques were used to modify some equations on the basis of maintaining the original physical phenomena while avoiding possible numerical issues associated with solving and evaluating the original equations. The model has the potential to be applied to both creep-ageing and pure-ageing processes for other aluminium alloys with similar creep and ageing behaviour. However, its application to other aluminium alloys that have different precipitation behaviour might have some limitations or require modification of the current model. Further study will be carried out on its applications.

7. Conclusions

A new unified constitutive model was developed to predict the experimentally observed creep-ageing behaviour of naturally aged Al-Cu-Li alloy AA2050-T34 during the creep age forming process. Quantitative analysis of precipitates for selected creep-aged samples has been carried out and the results were used to develop and calibrate the constitutive equations proposed in this study.

The equations relating microstructural variables to the yield strength of the alloy and its strengthening components were based on fundamental material ageing models for aluminium alloys, and some mathematical transformation techniques were used to eliminate possible numerical difficulties. Both softening from dissolving precipitates and hardening from new precipitates during creep-ageing of AA2050-T34 are simulated in the proposed model, as well as the strengthening resulting from dislocations and solutes. Good agreement was achieved between the experimental and predicted yield strength data.

The microstructural variables, including dislocation density, precipitate radius and solute concentration, play decisive roles in the creep-ageing behaviour of AA2050. They are all integrated into the creep model via a new creep variable. The

model successfully describes the recently observed double primary creep feature in AA2050-T34, and achieves good agreement with experimental results. The asymmetric tension/compression creep-ageing behaviour of the alloy was also predicted by the model, where different creep resistance occurs under tension and compression stress conditions.

Funding

This work was financially supported by the ESI Group (France) (Grant no. MESM_NEI065).

Acknowledgements

The authors would like to thank the financial support from ESI Group (France). The material was provided by Embraer (Brazil) and the specimens are machined through ESI Group. Their contributions are greatly appreciated. Mr Y. Li would also like to thank the support from the Chinese Scholarship Council (CSC) (Grant no. 201406320170).

Appendix A. Mathematical transformation of equations

The growth rate equation, Eq. (9) in Section 4.1.2, can be rewritten in a more general form as:

$$y = \frac{k}{x^n},\ (x>0, n>0) \tag{A1}$$

The equation has a numerical difficulty at $x = 0$. To avoid this difficulty, the denominator x^n needs to be converted to a numerator, i.e., from $y = f(x^{-n})$ to $y = f(x^n)$, while keeping its original characteristics.

Eq. (A1) is a concave, monotonically decreasing curve, which has a monotonically increasing gradient (dy/dx), as shown in Fig. A1(a). The simplest form of function $y = f(x^n)$ that has the same monotonicity and properties as Eq. (A1) is:

$$y = K|x|^m, (x<0, m>1) \tag{A2}$$

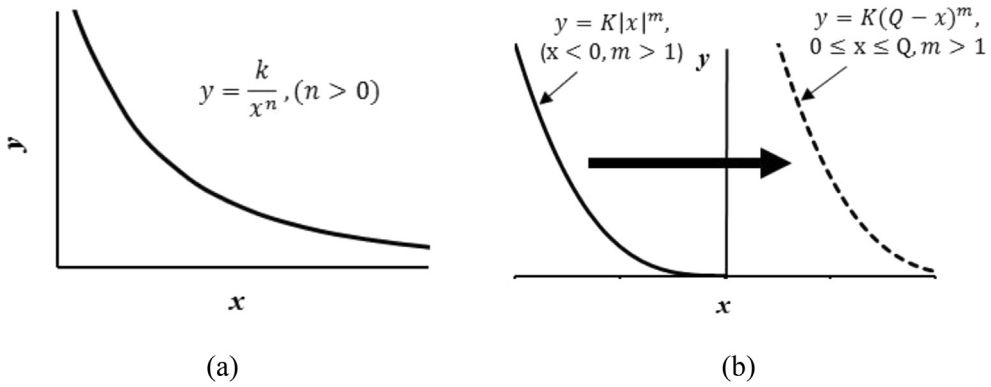

Fig. A1. Schematic showing the curves of the functions (a) $y = f(x^{-n})$ and (b) $y = f(x^n)$.

In order to obtain a similar range of parameter x in Eqs. (A1) and (A2), the curve of Eq. (A2) can be translated along x, as:

$$y = K(Q - x)^m, (0 \le x \le Q, m>1) \tag{A3}$$

Although a limit of Q exists for parameter x in Eq. (A3) which is different from that in Eq. (A1), it is reasonable when considering that x is the precipitate radius. The precipitates in alloys cannot grow infinitely, and Eq. (A3) sets a limit for its growth as Q.

In order to verify the effectiveness of the mathematical transformation. Both equations (considering the coarsening law with $n = 2$ for Eq. (A1)) have been used to model a set of precipitate evolution data obtained by (Decreus et al., 2013) for an Al-Cu-Li alloy artificially aged to slightly over-aged states. The material constants in both equations were determined by the optimisation technique introduced in Section 5.2 and are listed in Table A1. The results are illustrated in Fig. A2, and both curves correspond fairly with experimental data, while the transformed Eq. (A3) shows better fitting results in this particular condition.

Table A1
Material constants of Eqs. (A1) and (A3) in Fig. A2.

k	K	Q	m
0.026	0.275	1.06	1.11

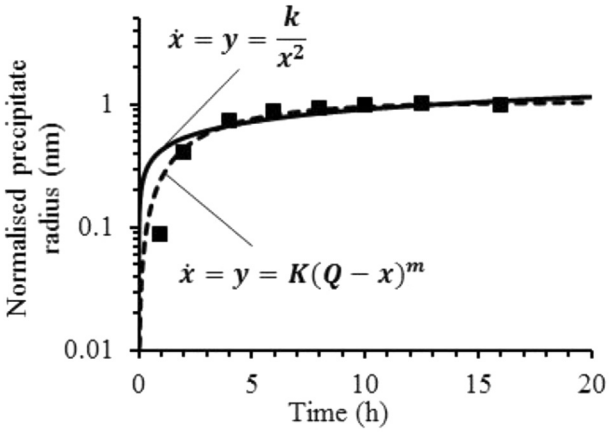

Fig. A2. Comparison of experimental (symbols) (Decreus et al., 2013) and numerical data from Eqs. (A1) (solid line) and (A3) (dashed line) of the normalised precipitate radius during ageing of an Al-Cu-Li alloy.

Similarly, for Eq. (23), since the denominator of $((\bar{r}_n)^{2n}+1)^2(\bar{r}_n)^{1-n}$ has similar monotonicity and properties compared to its simplified form, $\bar{r}_n^m$, the same mathematical technique discussed above can be used to transform it into Eq. (24). Fig. A3 compares the results of precipitation hardening calculated by Eqs. (23)–(25). All constants were fitted according to the precipitation related equations determined in Table 2 in Section 5.2 and listed in Table A2 below. All three curves show fairly consistent results with each other.

Table A2
Material constants for Eqs. (23) (24) and (25) in Fig. A3.

C_a	m_5	m_6	c	n	c'	n'	Q
180	0.65	5.5	850	1.9	0.329	0.01	1.1

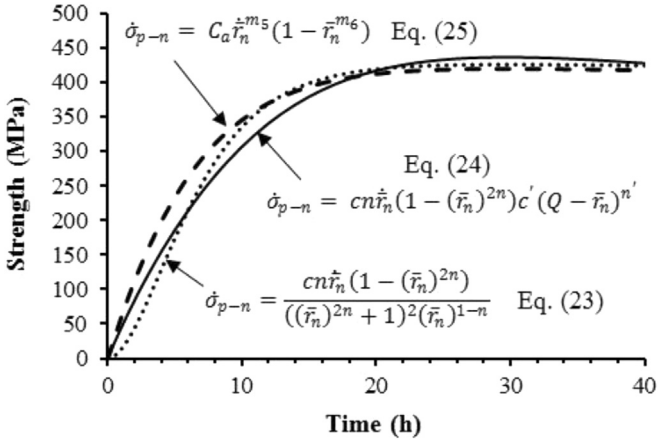

Fig. A3. Comparison of precipitation hardening results from Eq. (23) (dotted line), (24) (solid line) and (25) (dashed line) with material constants in Table A2.

Appendix B. Supplementary data

Supplementary data related to this article can be found at http://dx.doi.org/10.1016/j.ijplas.2016.11.007.

References

Aaron, H.B., Kotler, G.R., 1971. Second phase dissolution. Metall. Trans. 2, 393–408.
Abbena, E., Salamon, S., Gray, A., 2006. Modern Differential Geometry of Curves and Surfaces with Mathematica. CRC press.
Basirat, M., Shrestha, T., Potirniche, G.P., Charit, I., Rink, K., 2012. A study of the creep behavior of modified 9Cr–1Mo steel using continuum-damage modeling. Int. J. Plast. 37, 95–107.
Cassada, W., Shiflet, G., Starke, E., 1991. The effect of plastic deformation on Al2CuLi (T1) precipitation. Metall. Trans. A 22, 299–306.
Collins, D.M., Stone, H.J., 2014. A modelling approach to yield strength optimisation in a nickel-base superalloy. Int. J. Plast. 54, 96–112.
Decreus, B., Deschamps, A., De Geuser, F., Donnadieu, P., Sigli, C., Weyland, M., 2013. The influence of Cu/Li ratio on precipitation in Al–Cu–Li–x alloys. Acta Mater. 61, 2207–2218.
Donnadieu, P., Shao, Y., De Geuser, F., Botton, G.A., Lazar, S., Cheynet, M., de Boissieu, M., Deschamps, A., 2011. Atomic structure of T1 precipitates in Al–Li–Cu alloys revisited with HAADF-STEM imaging and small-angle X-ray scattering. Acta Mater. 59, 462–472.
El-Shennawy, M., Morita, Y., Kouso, M., 1999. Analytical and experimental investigation for tensile and compressive creep of the A3003P aluminium alloy used for plate-fin heat exchanger. JSME Int. J. Ser. A 42, 403–413.
Esmaeili, S., Lloyd, D., Poole, W., 2003a. Modeling of precipitation hardening for the naturally aged Al-Mg-Si-Cu alloy AA6111. Acta Mater. 51, 3467–3481.
Esmaeili, S., Lloyd, D., Poole, W., 2003b. A yield strength model for the Al-Mg-Si-Cu alloy AA6111. Acta Mater. 51, 2243–2257.
Estrin, Y., 1998. Dislocation theory based constitutive modelling: foundations and applications. J. Mater. Process. Technol. 80–81, 33–39.
Evans, R., 2000. A constitutive model for the high-temperature creep of particle-hardened alloys based on the θ projection method. Proc. R. Soc. Lond. Ser. A 456, 835–868.
Ho, K.C., Lin, J., Dean, T.A., 2004. Modelling of springback in creep forming thick aluminum sheets. Int. J. Plast. 20, 733–751.
Holman, M.C., 1989. Autoclave age forming large aluminum aircraft panels. J. Mech. Work. Technol. 20, 477–488.
Huang, C.-C., Wei, M.-K., Lee, S., 2011. Transient and steady-state nanoindentation creep of polymeric materials. Int. J. Plast. 27, 1093–1102.
Kelly, A., Nicholson, R.B., 1963. Precipitation hardening. Prog. Mater. Sci. 10, 151–391.
Kim, Y.-K., Kim, D., Kim, H.-K., Oh, C.-S., Lee, B.-J., 2016. An intermediate temperature creep model for Ni-based superalloys. Int. J. Plast. 79, 153–175.
Kocks, U., 1976. Laws for work-hardening and low-temperature creep. J. Eng. Mater. Technol. 98, 76–85.
Kocks, U.F., Argon, A.S., Ashby, M.F., 1975. Models for macroscopic slip. Prog. Mater Sci. 19, 171–229.
Kowalewski, Z., Hayhurst, D., Dyson, B., 1994. Mechanisms-based creep constitutive equations for an aluminium alloy. J. Strain Anal. Eng. Des. 29, 309–316.
Kumar, K., Brown, S., Pickens, J., 1996. Microstructural evolution during aging of an Al-Cu-Li-Ag-Mg-Zr alloy. Acta Mater. 44, 1899–1915.
Lam, A.C.L., Shi, Z., Yang, H., Wan, L., Davies, C.M., Lin, J., Zhou, S., 2015. Creep-age forming AA2219 plates with different stiffener designs and pre-form age conditions: experimental and finite element studies. J. Mater. Process. Technol. 219, 155–163.
Lequeu, P., Smith, K., Daniélou, A., 2010. Aluminum-copper-lithium alloy 2050 developed for medium to thick plate. J. Mater. Eng. Perform. 19, 841–847.
Li, B., Lin, J., Yao, X., 2002. A novel evolutionary algorithm for determining unified creep damage constitutive equations. Int. J. Mech. Sci. 44, 987–1002.
Li, C., Wan, M., Wu, X.-D., Huang, L., 2010. Constitutive equations in creep of 7B04 aluminum alloys. Mater. Sci. Eng. A 527, 3623–3629.
Li, H., Lin, J., Dean, T.A., Wen, S.W., Bannister, A.C., 2009. Modelling mechanical property recovery of a linepipe steel in annealing process. Int. J. Plast. 25, 1049–1065.
Li, Y., Shi, Z., Lin, J., Yang, Y.L., Huang, B.M., Chung, T.F., Yang, J.R., 2016a. Experimental investigation of tension and compression creep-ageing behaviour of AA2050 with different initial tempers. Mater. Sci. Eng. A 657, 299–308.
Li, Y., Shi, Z., Yang, Y.L., Lin, J., 2016b. Investigation of tensile and compressive creep behaviour of AA2050-T34 during creep age forming process. Key Eng. Mater. 716, 8.
Lifshitz, I.M., Slyozov, V.V., 1961. The kinetics of precipitation from supersaturated solid solutions. J. Phys. Chem. Solids 19, 35–50.
Lin, J., 2003. Selection of material models for predicting necking in superplastic forming. Int. J. Plast. 19, 469–481.
Lin, J., Dean, T.A., 2005. Modelling of microstructure evolution in hot forming using unified constitutive equations. J. Mater. Process. Technol. 167, 354–362.
Lin, J., Ho, K., Dean, T., 2006. An integrated process for modelling of precipitation hardening and springback in creep age-forming. Int. J. Mach. Tool. Manu 46, 1266–1270.
Lin, J., Liu, Y., 2003. A set of unified constitutive equations for modelling microstructure evolution in hot deformation. J. Mater. Process. Technol. 143–144, 281–285.
Lin, J., Yang, J., 1999. GA-based multiple objective optimisation for determining viscoplastic constitutive equations for superplastic alloys. Int. J. Plast. 15, 1181–1196.
Liu, G., Zhang, G., Ding, X., Sun, J., Chen, K., 2003. Modeling the strengthening response to aging process of heat-treatable aluminum alloys containing plate/disc-or rod/needle-shaped precipitates. Mater. Sci. Eng. A 344, 113–124.
Mitra, S., McLean, D., 1966. Work hardening and recovery in creep. Proc. R. Soc. Lond. Ser. A 295, 288–299.
Othman, A.M., Hayhurst, D.R., Dyson, B.F., 1993. Skeletal point stresses in circumferentially notched tension bars undergoing tertiary creep modelled with physically based constitutive equations. Proc. R. Soc. Lond. Ser. A 441, 343–358.
Prasad, N.E., Ramachandran, T.R., 2014. Chapter 3-Phase diagrams and phase reactions in Al–Li alloys. In: Prasad, N.E., Gokhale, A.A., Wanhill, R.J.H. (Eds.), Aluminum-lithium Alloys. Butterworth-Heinemann, Boston, pp. 61–97.
Raeisinia, B., Poole, W., Wang, X., Lloyd, D., 2006. A model for predicting the yield stress of AA6111 after multistep heat treatments. Metall. Mater. Trans. A 37, 1183–1190.
Reti, A., Flemings, M., 1972. Solution kinetics of two wrought aluminum alloys. Metall. Mater. Trans. B 3, 1869–1875.
Seidman, D.N., Marquis, E.A., Dunand, D.C., 2002. Precipitation strengthening at ambient and elevated temperatures of heat-treatable Al (Sc) alloys. Acta Mater. 50, 4021–4035.
Sherby, O.D., Burke, P.M., 1968. Mechanical behavior of crystalline solids at elevated temperature. Prog. Mater. Sci. 13, 323–390.
Shercliff, H.R., Ashby, M.F., 1990. A process model for age hardening of aluminium alloys—I. The model. Acta Metall. Mater. 38, 1789–1802.
Starink, M., Wang, S., 2003. A model for the yield strength of overaged Al–Zn–Mg–Cu alloys. Acta Mater. 51, 5131–5150.
Starke Jr., E.A., 1977. Aluminium alloys of the 70's: scientific solutions to engineering problems. An invited review. Mater. Sci. Eng. 29, 99–115.
Thomas, G., Whelan, M., 1961. Observations of precipitation in thin foils of aluminium+ 4% copper alloy. Philos. Mag. 6, 1103–1114.
Whelan, M.J., 1969. On the kinetics of precipitate dissolution. Met. Sci. 3, 95–97.
Wu, L., Ferguson, W.G., 2009. Modelling of precipitation hardening in casting aluminium alloys. Mater. Sci. Forum 618, 203–206.
Zhan, L., Lin, J., Dean, T.A., 2011a. A review of the development of creep age forming: experimentation, modelling and applications. Int. J. Mach. Tool. Manuf. 51, 1–17.
Zhan, L., Lin, J., Dean, T.A., Huang, M., 2011b. Experimental studies and constitutive modelling of the hardening of aluminium alloy 7055 under creep age forming conditions. Int. J. Mech. Sci. 53, 595–605.
Zhang, J., Deng, Y., Zhang, X., 2013. Constitutive modeling for creep age forming of heat-treatable strengthening aluminum alloys containing plate or rod shaped precipitates. Mater. Sci. Eng. A 563, 8–15.

Zhang, Q., Zhang, W., Liu, Y., 2015. Evaluation and mathematical modeling of asymmetric tensile and compressive creep in aluminum alloy ZL109. Mater. Sci. Eng. A 628, 340–349.
Zhao, Y., Fang, Q., Liu, Y., Wen, P., Liu, Y., 2015. Creep behavior as dislocation climb over NiAl nanoprecipitates in ferritic alloy: the effects of interface stresses and temperature. Int. J. Plast. 69, 89–101.
Zolochevsky, A., Voyiadjis, G.Z., 2005. Theory of creep deformation with kinematic hardening for materials with different properties in tension and compression. Int. J. Plast. 21, 435–462.